Acta Crystallographica Section D
Biological Crystallography
ISSN 0907-4449

High-pressure cryocooling for capillary sample cryoprotection and diffraction phasing at long wavelengths

Chae Un Kim,[a,b] Quan Hao[b] and Sol M. Gruner[a,c,d]*

[a]Field of Biophysics, Cornell University, Ithaca, NY 14853, USA, [b]MacCHESS, Cornell University, Ithaca, NY 14853, USA, [c]Cornell High Energy Synchrotron Source (CHESS), Cornell University, Ithaca, NY 14853, USA, and [d]Physics Department, Cornell University, Ithaca, NY 14853, USA

Correspondence e-mail: smg26@cornell.edu

Received 14 November 2006
Accepted 13 March 2007

PDB References: high-pressure cryocooled PPE, 2oqu, r2oqusf; high-pressure cryocooled thaumatin, 2oqn, r2oqnsf.

Crystal cryocooling is usually employed to reduce radiation damage during X-ray crystallography. Recently, a high-pressure cryocooling method has been developed which results in excellent diffraction-quality crystals without the use of penetrative cryoprotectants. Three new developments of the method are presented here: (i) Xe–He high-pressure cryocooling for Xe SAD phasing, (ii) native sulfur SAD phasing and (iii) successful cryopreservation of crystals in thick-walled capillaries without additional cryoprotectants other than the native mother liquor. These developments may be useful for structural solution of proteins without the need for selenomethionine incorporation and for high-throughput protein crystallography.

1. Introduction

Radiation damage, which often limits the room-temperature collection of complete macromolecular diffraction data sets, is conventionally mitigated by crystal cryocooling. The goal of cryoprotection is to lower the temperature of the crystal to below the protein glass-transition temperature with as little degradation of the crystal diffraction quality as possible. This often requires the incorporation of chemical cryoprotectants (Garman & Schneider, 1997). Practically, cryoprotectants that work well with one protein often do not work with another, requiring a trial-and-error search. Even when a suitable cryoprotectant is found, care has to be taken to avoid unwanted chemical reactions between the cyroprotectant and the protein, such as the binding of cryoprotectant to protein active sites.

Recently, Kim *et al.* (2005) reported an alternative procedure, high-pressure cryocooling, in which the use of penetrating cryoprotectants could be avoided by cryocooling protein crystals under high pressure. Exceptionally high quality diffraction data were obtained in terms of both diffraction resolution and crystal mosaicity. This method was successfully used in the study of the RCK domain of the KtrAB K^+ transporter (Albright *et al.*, 2006). High-pressure cryocooling was especially useful in this case since crystal cryoprotection and better quality diffraction could be achieved without perturbation of the ligand-binding site by cryoprotectants.

The high quality of the diffraction data from high-pressure cryocooled crystals enables a variety of diffraction-phasing procedures. High-pressure cryocooling was successfully extended to diffraction phasing of porcine pancreatic elastase (PPE) by incorporating krypton during the cryocooling process (Kim *et al.*, 2006). Even though the single Kr-binding

site was only 31% occupied, the quality of the diffraction allowed successful Kr SAD phasing. Intriguingly, the anomalous difference map created using the experimental PPE phases showed electron density (3.6σ level) at the S atoms naturally present in the protein, even though sulfur has an anomalous strength of only 0.18 electrons at the data-collection wavelength (0.86 Å). Since krypton SAD phasing was successful, the use of xenon in high-pressure cryocooling was of particular interest. Xenon has a stronger anomalous signal than krypton in the typical wavelength range for diffraction data collection (Schiltz *et al.*, 1994, 1997; Cohen *et al.*, 2001). Furthermore, it was estimated that xenon might be captured with higher occupancy in the high-pressure cryocooling, which would be very useful for SAD phasing (Kim *et al.*, 2006).

Here, we present three new results. (i) Xe–He high-pressure cryocooling followed by xenon SAD phasing was successfully demonstrated on PPE. (ii) Of greater interest is the demonstration of SAD phasing using the native sulfurs (Hendrickson & Teeter, 1981; Wang, 1985; Dauter *et al.*, 1999; Micossi *et al.*, 2002) of a thaumatin crystal prepared with He high-pressure cryocooling. (iii) Conventional wisdom holds that it is difficult to cryocool crystals in capillaries because the slow cooling rate leads to ice crystals. However, we demonstrated native sulfur phasing of a thaumatin crystal that was grown and the diffraction data were obtained in a thick-walled polycarbonate capillary. The entire capillary containing the crystal and mother liquor (no additional cryoprotectants) was successfully high-pressure cryocooled. Although the thermal mass of the capillary and surrounding bulk mother liquor resulted in relatively slow cryocooling of the sample, no ice rings were observed in the diffraction pattern. These results open new possibilities for high-throughput protein crystallography.

2. Experimental

2.1. Materials and sample preparation

2.1.1. Crystallization. Lyophilized PPE (catalog No. 20929) was purchased from SERVA (Heidelberg, Germany) and used without further purification. Crystallization experiments were carried out at 293 K using the hanging-drop vapor-diffusion technique. As described in Kim *et al.* (2006), 2 µl of a 25 mg ml^{-1} protein solution in pure water was mixed with 2 µl of a reservoir solution containing 30 m*M* sodium sulfate and 50 m*M* sodium acetate pH 5.0. Crystals (space group $P2_12_12_1$) appeared within a few days and crystals of dimensions 0.2 × 0.2 × 0.3 mm were used for Xe–He high-pressure cryocooling.

Thaumatin from *Thaumatococcus daniellii* was purchased from Sigma (Saint Louis, MO, USA; catalog No. T7638) and used for crystallization without further purification. Thaumatin crystallization was carried out at 293 K in a polycarbonate capillary with an inside diameter of 300 µm and a wall thickness of 300 µm (Gilero, Raleigh, NC, USA). Robust plastic capillaries were used to minimize capillary breakage, since this experiment was initiated as a study for high-throughput methodologies. Equal amounts of protein solution (25 mg ml^{-1} in 50 m*M* HEPES buffer pH 7.0) and reservoir solution containing 0.9 *M* sodium potassium tartrate were mixed. The mixed solution was then inserted into the polycarbonate capillary and the capillary was placed into a larger tube containing 0.9 *M* sodium potassium tartrate solution at the bottom. The large tube was carefully sealed with Parafilm to minimize evaporation of the crystallizing solution. The equilibrium between the capillary and the reservoir solution in the larger tube was reached by vapor diffusion. Crystals (space group $P4_12_12$) appeared within a few days and grew on the capillary inner surface (150 × 150 × 200 µm, truncated bipyramidal shape) in a few weeks.

2.1.2. High-pressure cryocooling. PPE crystals were prepared by Xe–He high-pressure cryocooling, which was modified from Kr–He high-pressure cryocooling as described in Kim *et al.* (2006). PPE crystals were first coated with NVH oil (Hampton Research) to prevent crystal dehydration and loaded into high-pressure tubes, which were then connected to the gas compressor. High-pressure cryocooling could not be carried out in a single step with the Xe–He mixture gas because Xe would solidify in the liquid-nitrogen-cooled bottom of the pressure tube and prevent the sample from falling (Sauer *et al.*, 1997; Schiltz *et al.*, 1997; Soltis *et al.*, 1997). Therefore, the crystals were initially pressurized with xenon gas to 1.0 MPa. After 15 min, the compressed xenon gas was released, liquid nitrogen (LN_2) was poured into the LN_2 bath of the cryocooling apparatus and the crystals were re-pressurized with helium. After 60 s, the helium pressure reached 145 MPa and the crystals were cryocooled to LN_2 temperature at 145 MPa pressure. Overall, the time from xenon-pressure release to cryocooling was about 150 s. The helium pressure was released 2 min after cryocooling and the crystals were transferred into a cryocap under liquid nitrogen for data collection.

Thaumatin crystals were prepared by the He high-pressure cryocooling process described in Kim *et al.* (2005). Briefly, the polycarbonate capillary containing crystals was cut into 2 cm lengths and loaded into the high-pressure cryocooling apparatus, which was then pressurized with helium gas to 170 MPa. The mother liquor around the crystals in the capillary was not removed so that the crystals were left fully hydrated; hence, oil coating to prevent crystal hydration was not needed. The capillary ends were left open under pressure, but water evaporation from the capillary during the brief process was negligible. No additional penetrating cryoprotectants were added to the mother liquor for high-pressure cryocooling. Once at high pressure, a magnetic constraint was released and the crystals fell down a length of high-pressure tubing into a zone kept at LN_2 temperature. The helium pressure was released and the crystals were subsequently handled at low temperature and ambient pressure for cryocrystallographic data collection.

As described in Kim *et al.* (2005), high-pressure cryocooling requires a minimum pressure of ∼100 MPa for crystal cryoprotection. Pressures higher than 100 MPa seem to have no significant effect on the crystal diffraction quality, at least for PPE and thaumatin. Therefore, the pressures of 145 and

170 MPa used for PPE and thaumatin sample preparations, respectively, were not controlled intentionally.

2.2. Data collection

Diffraction data were collected at the Cornell High Energy Synchrotron Source (CHESS) on beamline F2 (150 µm beam diameter, ADSC Quantum-210 CCD detector). In all cases, the detector face was perpendicular to the incident beam (2θ value of zero). All data were collected at 110 K (N_2 gas stream) and ambient pressure with an oscillation angle ($\Delta\varphi$) of 1.0° per image. In order to obtain useful anomalous signals from xenon and sulfur, the X-ray energy was located and calibrated at the Fe *K* edge (7.11 keV), where the anomalous strengths of xenon and sulfur are 9.0 and 0.7 e, respectively. Diffraction data were collected by the inverse-beam mode with a wedge of ten frames. The distance between the crystal and the detector was 65 mm for PPE and 95 mm for thaumatin. The exposure time for each frame was 2 min for PPE and 5 min for thaumatin. A total of 360 frames were collected from each crystal.

2.3. Data processing, phasing and model building

Data were indexed, pre-refined, integrated, post-refined, scaled and merged with *HKL*-2000 (Otwinowski & Minor, 1997) using the 'scale anomalous' flag to keep Bijvoet pairs separate. The initial structures were determined by the molecular-replacement method using *MOLREP* (Vagin & Teplyakov, 1997) from the *CCP*4 program suite (Collaborative Computational Project, Number 4, 1994). The structures were then refined against the data set with *REFMAC*5 (Murshudov *et al.*, 1997). In the PPE structure refinement, as the xenon occupancy and thermal *B* factor are highly correlated, the xenon occupancy was manually adjusted so that the refined thermal *B* factor of the Xe atom was close to the average

Table 1
Data-collection and refinement statistics for PPE and thaumatin.

Values in parentheses are for the highest resolution shell

	PPE	Thaumatin
High-pressure cryocooling	Xenon/helium	Helium
Wavelength (Å)	1.7463	1.7433
Space group	$P2_12_12_1$	$P4_12_12$
Unit-cell parameters (Å)		
a (Å)	50.2	58.0
b (Å)	58.2	58.0
c (Å)	74.7	150.7
Solvent content (%)	40.8	56.9
Mosaicity (°)	0.33	0.34
Resolution range (Å)	30–1.8 (1.86–1.8)	30–1.9 (1.97–1.9)
No. of observations	281537	469249
No. of unique reflections†	38238	38263
Multiplicity†	7.4 (6.6)	12.3 (3.5)
Completeness† (%)	97.7 (94.8)	99.4 (93.9)
R_{sym}† (%)	11.2 (26.8)	8.9 (17.5)
$I/\sigma(I)$	19.5 (4.6)	32.0 (5.0)
R factor (%)	17.8	17.6
R_{free} factor (%)	22.6	21.6
Average *B* factor (Å^2)	14.6	17.1
No. of water molecules	327	401
R.m.s. deviations from ideality		
Bond lengths (Å)	0.014	0.014
Angles (°)	1.387	1.322
Xenon occupancy	0.70	N/A
Xenon *B* factor (Å^2)	11.8	N/A

† The Bijvoet pairs were kept separate in the statistics.

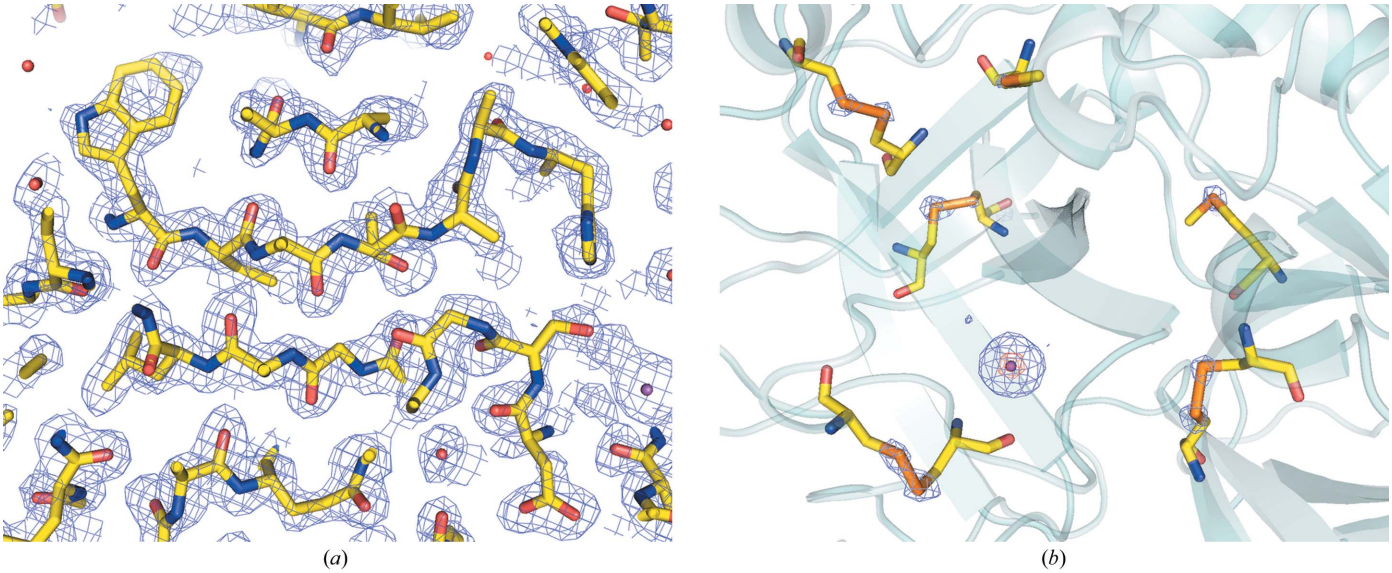

(*a*) (*b*)

Figure 1
Xe SAD phasing of PPE. (*a*) F_o electron-density map (1σ level) after Xe SAD phasing and density modification at 1.8 Å resolution. The final refined model solved by molecular replacement was superimposed for visual map evaluation. The figure of merit is 0.807 and the map correlation coefficient calculated with the final refined $2F_o - F_c$ density map is 0.83 for the main chain and 0.74 for side chains. (*b*) Anomalous difference map, contoured at the 4.5σ level, generated with the phases calculated from a single 0.70 occupancy xenon. The final refined model obtained using molecular replacement was superimposed to specify the origin of the peaks. Very strong density (red central peak contoured at 80σ) is found at the xenon site and ten additional peaks are assigned to S atoms that are naturally present in PPE. The electron-density peaks in a disulfide bond can be clearly distinguished. The anomalous strength of sulfur at the data-collection wavelength (1.7643 Å) is 0.70 e.

Table 2
SAD phasing statistics for PPE.

	Xe SAD phasing					Xe–S SAD phasing				
Resolution range (Å)	30–1.8	30–1.9	30–2.0	30–2.1	30–2.2	30–1.8	30–1.9	30–2.0	30–2.1	30–2.2
No. of unique reflections†	20337	17447	15040	13076	11434	20337	17447	15040	13076	11434
Estimated $\langle\lvert\Delta F\rangle/\langle F\rangle$ (%)	2.8	2.8	2.8	2.8	2.8	3.0	3.0	3.0	3.0	3.0
Experimental $\langle\lvert\Delta F\rangle/\langle F\rangle$ (%)	4.6	4.4	4.2	4.1	4.0	4.6	4.4	4.2	4.1	4.0
Experimental $\langle\lvert\Delta F\rangle/\sigma\langle\Delta F\rangle$	0.89	1.01	1.09	1.15	1.20	0.89	1.01	1.09	1.15	1.20
FOM after *DM*	0.807	0.821	0.800	0.775	0.767	0.824	0.837	0.809	0.797	0.807
No. of residues found	232	230	178	35	8	234	235	228	122	51
No. of residues docked in sequence	232	230	133	0	0	234	235	228	21	0
Map correlation coefficient for main chain	0.83	0.81	0.78	0.74	0.70	0.85	0.83	0.80	0.76	0.71
Map correlation coefficient for side chains	0.74	0.71	0.68	0.64	0.61	0.76	0.74	0.71	0.67	0.63
R factor (%)	22.5	22.3	24.3	20.7	18.8	21.6	21.8	23.0	21.8	19.0
Connectivity index	0.97	0.97	0.91	0.75	0.57	0.97	0.98	0.95	0.86	0.74

† The Bijvoet pairs were merged in the statistics.

thermal *B* factor of the crystallographically refined main-chain atoms. In SAD phasing, the anomalous scattering substructure was initially solved and refined using the programs *SAPI* (Hao *et al.*, 2003) and *ABS* (Hao, 2004). In PPE, one Xe atom was found in the previously reported site (Schiltz *et al.*, 1997; Mueller-Dieckmann *et al.*, 2004). All 17 sulfur sites in thaumatin (eight disulfide pairs and one S atom of a methionine residue) were located. The heavy-atom positions were then input into *OASIS*-2004 (Wang *et al.*, 2004) for SAD phasing. Afterwards, density modification was performed using *DM* (Cowtan, 1994). Auto model building was performed with *ARP*/*wARP* (Perrakis *et al.*, 1999) and *REFMAC*5 (Murshudov *et al.*, 1997) was used for refinement. The electron-density maps and structural images were generated using *PyMOL* (DeLano, 2002).

3. Results

3.1. Porcine pancreas elastase

The crystallographic data statistics of the PPE crystal prepared by Xe–He high-pressure cryocooling are summarized in Table 1. The mosaicity of the Xe–He high-pressure cryocooled PPE crystal was 0.33°, whereas the mosaicity of conventionally (ambient pressure) flash-cryocooled PPE crystals without penetrating cryoprotectants was approximately 1° (Kim *et al.*, 2006). This indicates that crystal cryoprotection was successfully achieved by Xe–He high-pressure cryocooling. The resolution limit (1.8 Å) seemed to be poorer than that of Kr–He high-pressure cryocooled crystals (1.3 Å), but this was mainly a consequence of the increased absorption and relatively weak beam intensity at the longer data-collection wavelength (1.7463 Å). The crystallographic structure was solved by the molecular-replacement method using the known structure 1c1m (Prangé *et al.*, 1998). In the final refined model the occupancy of xenon was refined to be 0.70, which is much higher than the occupancy of krypton (0.31) reported by Kim *et al.* (2006). Since the anomalous strength of xenon at 1.7463 Å is 9.0 e, a single 0.70 occupancy xenon site in PPE (240 residues, 26 kDa) gave an estimated Bijvoet amplitude ratio ($\langle\lvert\Delta F\rvert\rangle/\langle F\rangle$) of 2.8%.

Xe SAD phasing was then carried out without the use of the known protein structure. The F_o map (Fig. 1*a*) was generated at 1.8 Å resolution and the final refined model solved using the molecular-replacement method was superimposed to visually evaluate the map quality. The map correlation coefficients between the F_o map and the $2F_o - F_c$ map from the final refined model for the main chain and side chains were 0.83 and 0.74, respectively. In the auto model-building process, 97% of the total residues (232 out of 240) could be found and docked in the electron density. In order to investigate the effect of resolution on the SAD phasing, the 1.8 Å data set was cut off at resolutions of 1.9, 2.0, 2.1 and 2.2 Å. Auto model building was straightforward up to 1.9 Å and a partial structure could be found and docked at 2.0 Å. In the anomalous difference map (Fig. 1*b*), a very strong peak (central peak >80σ) was observed at the xenon site. Additionally, all ten sulfurs (anomalous strength of 0.7 e at 1.7643 Å) that are naturally present in PPE were visible at 4.5σ, with peak heights ranging up to 7σ. These S atoms were included for SAD phasing and Xe–S SAD phasing was carried out at various resolution limits. Overall, the phase quality was slightly improved compared with Xe SAD phasing, so that auto model building was straightforward up to 2.0 Å and a partial structure could be found and docked at 2.1 Å. Details of Xe SAD phasing and Xe–S SAD phasing are summarized in Table 2.

3.2. Thaumatin

As shown in Fig. 2(*a*), the entire cryocooled sample looked clear, including a crystal and mother liquor in the capillary. The crystal diffraction (Fig. 2*b*) showed no crystalline ice rings, which confirms that amorphous ice formed inside the capillary on He high-pressure cryocooling. In contrast, ambient-pressure flash-cryocooling of capillary samples resulted in crystalline ice rings.

The crystallographic data statistics of the thaumatin crystal are summarized in Table 1. The refined crystallographic structure was solved by the molecular-replacement method using the known structure 1lxz (Charron *et al.*, 2002). Using the calculated phases, the anomalous difference map (Fig. 2*c*) was generated at 1.9 Å to check the anomalous signals from S

atoms. In the map, all 17 sulfurs could be clearly distinguished and the maximum peak height was higher than 10σ at most of the sulfur sites.

S SAD phasing was then carried out to see if the diffraction could be phased without a known structure. In the anomalous substructure, all 17 S-atom positions could be resolved at 1.9 Å resolution. The map correlation coefficients between the F_o map (Fig. 2*d*) at 1.9 Å and the $2F_o - F_c$ map from the final refined model were 0.82 for the main chain and 0.75 for the side chains. In the auto model-building process, 95% of the total residues (197 out of 207) could be found and docked in the electron density. S SAD phasing at different resolutions was straightforward up to 2.1 Å and a partial structure could be found and docked at 2.2 and 2.3 Å. Details of S SAD phasing are summarized in Table 3.

4. Discussion

To date, high-pressure cryocooling without added penetrative cryoprotectants has been applied to various protein crystals,

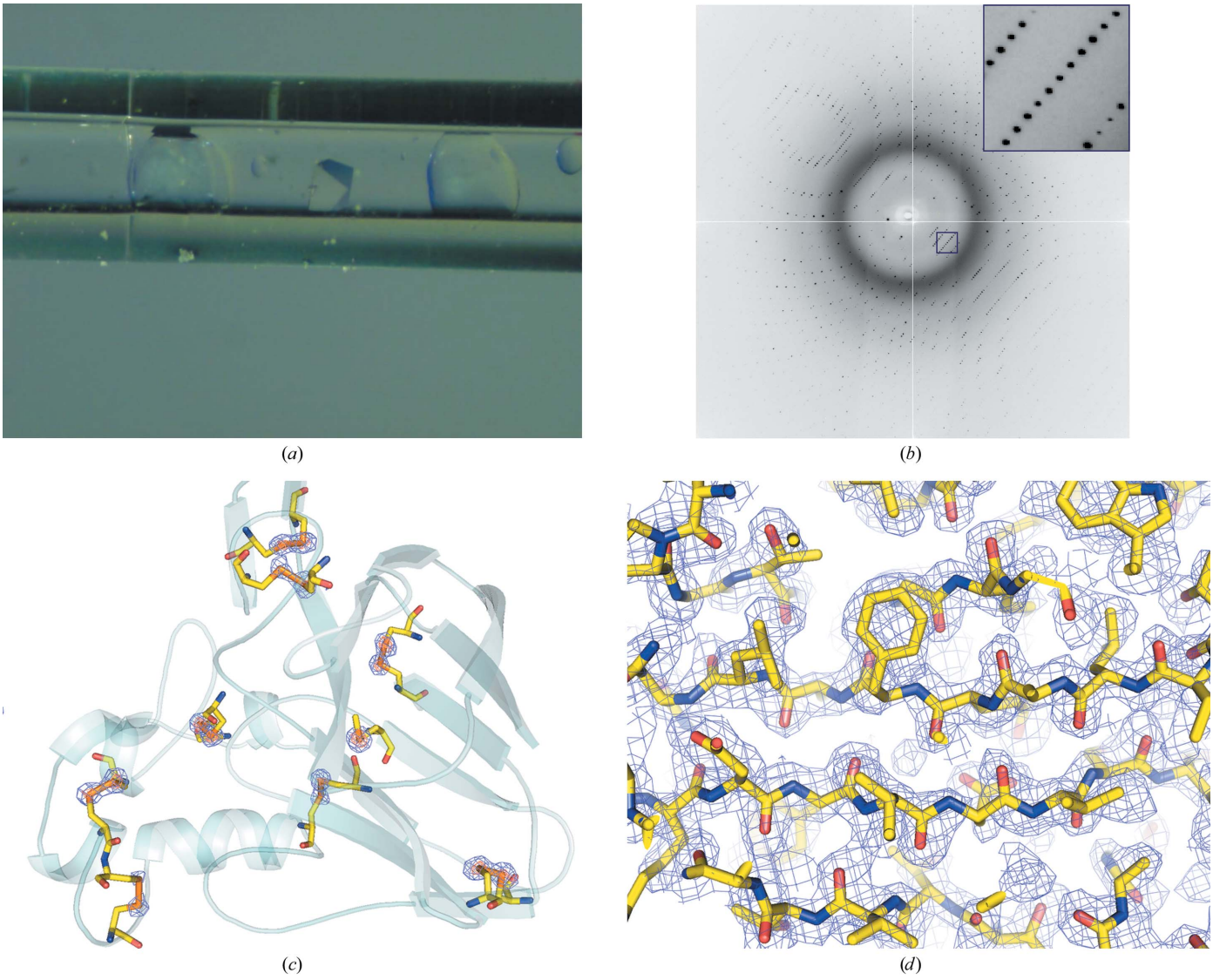

Figure 2
He high-pressure cryocooling and S SAD phasing of thaumatin. (*a*) Thaumatin crystal in a polycarbonate capillary at 110 K. The entire sample, the crystal and mother liquor in the capillary, was He high-pressure cryocooled without adding penetrative cryoprotectants. This clear sample could not be obtained by conventional (room-pressure) flash-cryocooling when cryoprotectants were not added. (*b*) Diffraction image of the thaumatin crystal grown in a polycarbonate capillary that was He high-pressure cryocooled at 170 MPa. The diffuse background scatter from the capillary ranges from 4.5 to 5.5 Å. The lack of ice rings on the image confirms that water vitrification was successfully achieved under high pressure. The resolution limit [$I/\sigma(I) \simeq 5.0$] is approximately 1.9 Å and the crystal mosaicity is 0.34°. The diffraction spots in the enlarged region look compact. (*c*) Anomalous difference map (5σ level) generated with the refined phases. All 17 sulfurs that naturally present in thaumatin are clearly visible. The shape of the electron density at disulfide bonds is dumbbell-shaped, so two-sulfur positions could be easily distinguished. The peak height was over the 10σ level (red) for most of the sulfur sites and the peak at Met112 was even visible at the 15σ level. (*d*) F_o electron-density map (1σ level) after S SAD phasing and density modification at 1.9 Å resolution. The final refined model solved by molecular replacement was superimposed for visual map evaluation. The figure of merit is 0.824 and the map correlation coefficient calculated with the final refined $2F_o - F_c$ density map is 0.85 for the main chain and 0.76 for side chains.

Table 3
S SAD phasing statistics for thaumatin.

Resolution range (Å)	30–1.9	30–2.0	30–2.1	30–2.2	30–2.3	30–2.4
No. of unique reflections†	20909	18143	15756	13764	12099	10680
Estimated $\langle\lvert\Delta F\rvert\rangle/\langle F\rangle$ (%)	1.4	1.4	1.4	1.4	1.4	1.4
Experimental $\langle\lvert\Delta F\rvert\rangle/\langle F\rangle$ (%)	2.1	1.7	1.5	1.5	1.4	1.4
Experimental $\langle\lvert\Delta F\rvert\rangle/\sigma\langle\Delta F\rangle$	0.64	0.70	0.75	0.78	0.81	0.84
FOM after *DM*	0.794	0.747	0.785	0.756	0.780	0.783
No. of residues found	197	194	192	175	166	60
No. of residues docked in sequence	197	194	192	121	93	0
Map correlation coefficient for main chain	0.82	0.79	0.78	0.75	0.74	0.71
Map correlation coefficient for side chains	0.75	0.73	0.72	0.70	0.69	0.68
R factor (%)	23.9	24.6	23.6	22.0	23.2	22.3
Connectivity index	0.96	0.96	0.95	0.92	0.91	0.76

† The Bijvoet pairs were merged in the statistics.

resulting in high-quality diffraction. It should be emphasized that high-pressure cryocooling mainly mitigates damage during the cryocooling process. The resultant diffraction quality is limited by the initial crystal quality prior to being frozen.

In high-pressure cryocooling, oil coating was an important step to prevent crystal dehydration in the high-pressure gas prior to cooling. However, in some cases it has been observed that crystals are degraded by the oil itself before the completion of high-pressure cryocooling. In this case, crystal encapsulation in a capillary is an alternative way to prevent crystal dehydration, as shown in the case of thaumatin. This result is surprising because vitrification of the capillary sample was impossible by flash-cryocooling at ambient pressure, regardless of the precipitant concentration at least up to 1.5 *M*, when no cryoprotectants were added. For comparison, several capillary samples were made with various amount of glycerol as a cryoprotectant agent, keeping the sodium potassium tartrate concentration constant at 0.9 *M*. It was observed that more than 13%(*v*/*v*) glycerol was required to make a visually transparent capillary sample upon plunging into an LN_2 bath at ambient pressure.

This result may have a significant impact on high-throughput crystallography. Although huge efforts are being expended to automate the screening/crystallization steps and data collection, the process of harvesting crystals and cryocooling is still performed manually. High-pressure cryocooling may play a key role in these steps by allowing a completely automated crystallography pipeline where crystals are screened and grown in capillaries, the capillaries are high-pressure cryocooled for cryoprotection, the vitrified samples are automounted and complete data sets are collected.

For this purpose, the physical constraints for high-pressure cryocooling capillary samples need to be carefully investigated. It was observed that crystalline ice in the surrounding mother liquor was sometimes not suppressed under pressure: in experiments on thaumatin, some capillaries prepared by high-pressure cryocooling were not successfully vitrified. Pure water in a polycarbonate capillary was not vitrified by high-pressure cryocooling, suggesting that an appropriate precipitant concentration was required to facilitate amorphous ice formation. It is known that the formation of amorphous ice generally requires a very fast cooling rate (Kriminski *et al.*, 2003). However, the cooling rate of a capillary sample is limited by the large thermal mass of the thick-walled capillary and the mother liquor inside the capillary. Use of thinner, lower thermal mass capillaries such as polyethylene terephthalate tubing (Kalinin & Thorne, 2005) would increase the cooling rate and may result in a higher percentage of successfully high-pressure cryocooled samples. On the other hand, adding a minimal amount of cryoprotecting agents to the capillary samples should also be carefully tested to determine whether combining chemical cryoprotectants and high-pressure cryocooling would produce better results for capillary samples.

Compared with Kr–He high-pressure cryocooling (Kim *et al.*, 2006), Xe–He high-pressure cryocooling has additional benefits for diffraction phasing. This report shows that a higher occupancy of Xe was obtained for PPE at a lower applied Xe pressure (a Kr pressure of 10 MPa resulting in 0.31 occupancy compared with a Xe pressure of 1 MPa resulting in 0.70 occupancy). These results are consistent with the estimation from previous reports (Schiltz *et al.*, 1994, 1997). Additionally, xenon has stronger anomalous signals than krypton in most of the practical data-collection wavelength range: the anomalous scattering strength of xenon gradually increases from 3.4 e at the Se *K* absorption peak (0.98 Å) to 11.8 e at Cr *Kα* (2.29 Å), whereas that of krypton at its *K* absorption peak (0.87 Å) is only 3.8 e. For PPE, the anomalous signal used for Xe SAD phasing was approximately five times stronger than that used for Kr SAD phasing. Therefore, partial auto model building was possible with a lower cutoff resolution data set (30–2.0 Å) in Xe SAD phasing. In Kr SAD phasing, model autobuilding had difficulty in finding residues using a 30–1.8 Å resolution data set.

If there are no noble gas binding sites, then high-pressure cryocooling can simply be used for crystal cryoprotection and S SAD phasing can be tried if high-quality diffraction is available and the anomalous signal from S atoms is sufficient, as in the thaumatin case. Alternatively, high-pressure cryocooling can be combined with most other existing methods for experimental phasing such as SeMet synthesis and heavy-atom solution soaks.

In summary, Xe–He high-pressure cryocooling was applied to PPE and Xe SAD phasing was successfully carried out. The anomalous signal from xenon captured by Xe–He high-pressure cryocooling was stronger than that of krypton captured by Kr–He high-pressure cryocooling. He high-pressure cryocooling was applied to successfully cryocool a thaumatin crystal and mother liquor in a capillary. Surprisingly, the entire system could be vitrified, although the cooling rate was relatively slow. The diffraction quality was sufficiently good that S SAD phasing could successfully be achieved. These results demonstrate that high-pressure cryocooling opens

novel possibilities in specimen preparation for macromolecular crystallography.

We thank Buz Barstow, Nozomi Ando, Yi-Fan Chen and the MacCHESS staff for assistance in data collection, Gil Toombes and Qun Liu for useful comments and assistance in data analysis and George T. DeTitta, Michael G. Marlowski, Joseph R. Luft and HWI scientists for encouragement. This work was supported by US NIH grant GM074899 and the MacCHESS grant (US NIH grant RR 001646) and by US DOE grant DE-FG02-97ER62443 and CHESS, which is supported by the US NSF and NIH-NIGMS through NSF grant DMR-0225180.

References

Albright, R. A., Vazquez Ibar, J.-L., Kim, C. U., Gruner, S. M. & Morais Cabral, J. H. (2006). *Cell*, **126**, 1147–1159.
Charron, C., Kadri, A., Robert, M.-C., Giegé, R. & Lorber, B. (2002). *Acta Cryst.* D**58**, 2060–2065.
Cohen, A., Ellis, P., Kresge, N. & Soltis, S. M. (2001). *Acta Cryst.* D**57**, 233–238.
Collaborative Computational Project, Number 4 (1994). *Acta Cryst.* D**50**, 760–763.
Cowtan, K. (1994). *Jnt CCP4/ESF–EACBM Newsl. Protein Crystallogr.* **31**, 34–38.
Dauter, Z., Dauter, M., de La Fortelle, E., Bricogne, G. & Sheldrick, G. M. (1999). *J. Mol. Biol.* **289**, 83–92.
DeLano, W. L. (2002). *PyMOL.* DeLano Scientific, San Carlos, CA, USA.
Garman, E. F. & Schneider, T. R. (1997). *J. Appl. Cryst.* **30**, 211–237.
Hao, Q. (2004). *J. Appl. Cryst.* **37**, 498–499.
Hao, Q., Gu, Y.-X., Yao, J.-X., Zheng, C.-D. & Fan, H.-F. (2003). *J. Appl. Cryst.* **36**, 1274–1276.
Hendrickson, W. A. & Teeter, M. M. (1981). *Nature (London)*, **290**, 107–113.
Kalinin, Y. & Thorne, R. (2005). *Acta Cryst.* D**61**, 1528–1532.
Kim, C. U., Hao, Q. & Gruner, S. M. (2006). *Acta Cryst.* D**62**, 687–694.
Kim, C. U., Kapfer, R. & Gruner, S. M. (2005). *Acta Cryst.* D**61**, 881–890.
Kriminski, S., Kazmierczak, M. & Thorne, R. E. (2003). *Acta Cryst.* D**59**, 697–708.
Micossi, E., Hunter, W. N. & Leonard, A. G. (2002). *Acta Cryst.* D**58**, 21–28.
Mueller-Dieckmann, C., Polentarutti, M., Djinovic Carugo, K., Panjikar, S., Tucker, P. A. & Weiss, M. (2004). *Acta Cryst.* D**60**, 28–38.
Murshudov, G. N., Vagin, A. A. & Dodson, E. J. (1997). *Acta Cryst.* D**53**, 240–255.
Otwinowski, Z. & Minor, W. (1997). *Methods Enzymol.* **276**, 307–326.
Perrakis, A., Morris, R. & Lamzin, V. S. (1999). *Nature Struct. Biol.* **6**, 458–463.
Prangé, T., Schiltz, M., Pernot, L., Colloc'h, N., Longhi, S., Bourguet, W. & Fourme, R. (1998). *Proteins*, **30**, 61–73.
Sauer, O., Schmidt, A. & Kratky, C. (1997). *J. Appl. Cryst.* **30**, 476–486.
Schiltz, M., Prangé, T. & Fourme, R. (1994). *J. Appl. Cryst.* **27**, 950–960.
Schiltz, M., Shepard, W., Fourme, R., Prangé, T., de La Fortelle, E. & Bricogne, G. (1997). *Acta Cryst.* D**53**, 78–92.
Soltis, S. M., Stowell, M. H. B., Wiener, M. C., Phillips, G. N. Jr & Rees, D. C. (1997). *J. Appl. Cryst.* **30**, 190–194.
Vagin, A. & Teplyakov, A. (1997). *J. Appl. Cryst.* **30**, 1022–1025.
Wang, B.-C. (1985). *Methods Enzymol.* **115**, 90–112.
Wang, J.-W., Chen, J.-R., Gu, Y.-X., Zheng, C.-D., Jiang, F. & Fan, H.-F. (2004). *Acta Cryst.* D**60**, 1987–1990.